applied sciences

MDPI

Article

Estimation of Sedimentary Rock Porosity Using a Digital Image Analysis

Qianhao Tang * and Ivan Gratchev

School of Engineering and Built Environment, Griffith University, Southport, QLD 4222, Australia
* Correspondence: qianhao.tang@griffithuni.edu.au

Abstract: Pore space characterisation is important in assessing the strength and hydraulic characteristics of rock. This paper proposes a new relationship to estimate the porosity of natural rocks using the data from a scanning electron microscope (SEM) and a pore and crack analysis system (PCAS). The obtained results were compared with the data obtained from a series of conventional mercury intrusion porosimetry (MIP) experiments. Three different rocks, namely siltstone, sandstone, and coal, collected from a depth below 400 m, were investigated in this study. The results indicated that the proposed method of digital analysis could accurately identify the pore size and porosity values, which were in agreement with the experimental data. The relationship between the two-dimensional porosity estimated from the digital analysis and the three-dimensional porosity obtained from laboratory experiments was established. A few limitations on the use of the proposed method have also been identified and discussed.

Keywords: porosity; pore size distribution; digital image analysis; sandstone; sedimentary rock; PCAS

check for updates

Citation: Tang, Q.; Gratchev, I. Estimation of Sedimentary Rock Porosity Using a Digital Image Analysis. *Appl. Sci.* **2023**, *13*, 2066. https://doi.org/10.3390/app13042066

Academic Editor: Giuseppe Lacidogna

Received: 13 January 2023
Revised: 25 January 2023
Accepted: 3 February 2023
Published: 5 February 2023

Copyright: © 2023 by the authors. Licensee MDPI, Basel, Switzerland. This article is an open access article distributed under the terms and conditions of the Creative Commons Attribution (CC BY) license (https://creativecommons.org/licenses/by/4.0/).

1. Introduction

A number of studies in the past decade have shown that porosity and pore size can significantly affect the physical properties of rocks [1–5]. Previous research established a few relationships between porosity, Young's modulus, and strength of rock [1–4,6,7]. However, Chang et al. [8] reviewed 31 empirical correlations between rock properties and porosity and noted that the majority of these empirical equations were not sufficiently general as they had strong regional influences, and were unable to account for all available published data on rock strength and physical properties.

In current practices, laboratory methods are employed to investigate the rock pore space, yet provide different levels of accuracy. Mercury intrusion porosimetry (MIP) is a standardized technique that enables precise estimations of the pore size of rock in the laboratory [9]. However, this experimental procedure is time-consuming, and it requires special equipment that may not be readily available in many laboratories around the world. The scanning electron microscope (SEM) method is an alternative approach that requires minimal sample preparation [10]. Although rock often appears as continuous material, at a microscopic scale, it is composed of a sequence of particles and pores that constitute a rock structure. Thus, using high-quality SEM images, it is possible to identify and quantify the open pore space in rock, which can provide an estimation of the material porosity [11–13]. Yet, recent works [13–15] indicated that due to the diversity of rock structures, the quality of digital photographs, and the complexity of the numerical recognition algorithm, it has been extremely challenging to detect and analyse each pore fracture in SEM images to a high level of accuracy. In this regard, the consequential outcome of studies using a digital analysis method of morphological fracture is limited, and only a few practical approaches for the fracture image recognition have been proposed to date [14]. One of them is the pore and crack analysis system (PCAS), which has recently become a popular tool to quantify the fracture and pore space in SEM images [16–21]. As it provides the advantages of

simplicity and efficiency over conventional manual procedures, PCAS has successfully been employed to detect cracks, micropores, and mineral particles in rock or soil [22,23]. However, recent studies indicate some discrepancies between the experimentally measured three-dimensional porosity and the two-dimensional porosity obtained from the digital image analysis. The summary of the previous research presented in Table 1 clearly shows relatively large differences in the porosity values (ranging from 0.56 to 4.6) obtained from the same material using either a direct experimental method or the digital analysis technique. It is clear that more research is necessary to clarify the existing correlations and to develop guidelines on the use of digital analysis for the estimation of rock porosity.

Table 1. Summary of previous research on porosity using MIP and digital analysis methods.

Rock/Soil	Porosity, %		Ratio, n_e/n_d	References
	Experiment, n_e	Digital Analysis, n_d		
Mudstones	6.5	1.4	4.6	Loucks et al. [15]
Sandstone	8.72	9.27	0.94	Desbois et al. [24]
Carbonate rock	7.9	14.2	0.56	Bera et al. [25]
Shale	3.5 3.4	2.75 2.74	1.27 1.24	Klaver et al. [26]
Sandstone	21.84	21.64	1	Guan et al. [27]
Hardened Cement paste	10–25	5.56–20	1.8–1.25	Lyu et al. [28]
Carbonate rock	22.83 28.04	22.70 25.53	1 1.10	Sun et al. [29]
Mancos shale	1.1 1.1	0.5 0.4	2.2 2.4	Goral et al. [30]
Sandstone	8–12	8.2	1.21	Niu et al. [31]

This article seeks to establish the relationship between the porosity obtained via the MIP and digital analysis methods, which can be widely used for different sedimentary rocks. A series of MIP experiments were carried out on three common sedimentary rocks (sandstone, siltstone, and coal). The porosity and pore size distribution of these rocks were estimated from the high-quality SEM images by employing the PCAS approach. This paper presents and discusses the obtained results.

2. Materials and Methods

2.1. Rocks Used

Core samples of fresh sandstone, siltstone, and coal were collected from depths of 400–500 m in southeast Shanxi Province, China. All three sedimentary rocks were part of the Lower Permian Shanxi Formation. It is well known that the rock structure, which determines the physical properties of rock, may vary depending on the geological origin and level of weathering [32]. Deep underground rocks are typically less affected by external weathering factors, and for this reason, they may remain fresh under greater pressures which cause the development of mineral grains that have a more pronounced effect on the engineering properties [33].

Block specimens of 1 cm^3 and specimens of flake shapes were utilised for MIP testing and SEM analysis. The mineralogical composition and density of each rock are given in Table 2. The coal rock was much lighter than the sandstone and siltstone, with an average density of 1.3 g/cm^3.

Table 2. Description and mineral composition of the sandstone, siltstone, and coal.

Rock	Description	Mineralogy	Density (g/cm^3)
Sandstone	Light grey colour, grain size fine to medium, massive texture, no visible cracks	Quartz Calcium Carbonate Kaolinite	2.65
Siltstone	Grey colour, fine-grained, massive texture, and no visible cracks	Quartz Kaolinite	2.60
Coal	Black colour, fine-grained, nonelastic, massive texture, and minor visible cracks	Carbon Calcium Carbide Calcium Carbonate	1.30

2.2. X-ray Diffraction Analysis

To identify the mineral composition of sandstone, siltstone, and coal, XRD analysis was performed on powdered samples using the Cu K-alpha radiation wavelength of 1.541 Å. The diffraction pattern was recorded using a step scale of 0.02 and measured in 2θ with a range of 5–90. The X-ray diffractometer exported the X-ray pattern in a text format, which was then imported into Excel. The peaks' positions in 2θ and intensities in the XRD plots were used to identify the minerals [34]. The X-ray data showed that the quartz was the main mineral in both sandstone and siltstone, with minor presence of kaolinite. The coal mainly consisted of carbon (Table 2).

2.3. Scanning Electron Microscope (SEM)

The microstructural characteristics of rock surfaces were identified using the JEOL JSM 7800F scanning electron microscope. The water in the sample was removed by vacuum. Using a concentrated electron beam, the SEM performed a point-by-point scan across the specimen surface. Because the rock sample is non-conductive, its surface was covered with a layer of Au. The current released by the electron beam stimulated the sample's surface, created backscattered electrons, and reached the display through signal collecting and signal conversions. The sensor received fewer reflected electrons from flat and depressed areas, causing the image to appear dark, and more reflected electrons from relatively steep and elevated areas, causing the image to appear brighter. The surface topography of the sample was then microscopically defined and measured. A range of magnifications from 500× to 40,000× was used to investigate the rock structure and pore space. Ninety images that covered the entire surface were collected. The images with a magnification of 1000× were used for PCAS analysis.

2.4. Mercury Intrusion Porosimetry (MIP) Tests

A series of MIP tests were conducted following the Chinese standard GB/T 21560.1 [35] with Mercury Intrusion Porosimeter Autopore VI (Figure 1). The specimen had a block shape with a size of 1 cm^3. Prior to testing, the specimens were dried in an oven at 105° C for at least 48 h, and then cooled at a room temperature of 25 °C. The pressure applied and pore diameter sizes ranged from 0.001 MPa to 400 MPa and 3 nm to 900,000 nm, respectively. As mercury is a non-invasive liquid, it can only enter the pore space under the action of external pressures. Therefore, the pore diameter d (nm) can be related to the applied pressure (P, MPa), as given in Equation (1).

$$D = -4\gamma cos\theta/P \quad (1)$$

where γ is the surface tension of mercury (0.45 N/m), and θ is the contact angle of mercury (130°). When the sample aperture is idealised as a smooth and step-changing cylinder, the

liquid–solid interface area (S) can be expressed in relation to the length L, and the changing volume (ΔV) as given in Equation (2):

$$S = L^{*}d^{*}\pi = 4\Delta V/d \quad (2)$$



Figure 1. Micromeritics autopore mercury intrusion porosimeter.

When computing the pore size distribution, the *DV/Dd* and *DV/Dlogd* values are compared to the pore size on the y-axis, and thus the pore distribution and size may be assessed. *DV/Dd* is commonly utilised for analysing minor pore size changes [36]. When the distribution of voids is wider, or the pore size is greater than tens of nanometres, the logarithmic relationship is applied (Equation (3)).

$$DV/Dlogd = ln10^{*}d^{*}(DV/Dd) \quad (3)$$

2.5. Pore and Crack Analysis System (PCAS)

PCAS image analysis software is a specialised tool for a quantitative pore system analysis. It can locate different pores and cracks in an image and extract different geometric and statistical information. For simplicity, the length was measured in nm. The true length (D) can be converted to pixel length (Dp) by the following formula (Equation (4)):

$$D/D_p = R \quad (4)$$

where R is the resolution of SEM images, which is approximately 93 nm units per pixel for a magnification of 1000× in SEM images.

The SEM image consists of pixels with different greyscale levels ranging from 0 (white) to 255 (black). By selecting an appropriate greyscale threshold (T), pores and particles in the image can be identified. A pixel that represents a pore is selected as a reference for its characteristic greyscale level value of X. Then, for any pixel point in an image, it can be analysed using Equation (5):

$$X' - X = d \quad (5)$$

where X' is the current pixel point of a greyscale value, and d is the greyscale value difference between the reference pixel point and the current pixel point. Then, the comparisons

with the greyscale threshold (T) can be made: if *d* is less than T, then the pixel point is recognised as a pore; otherwise, the pixel point would be recognised as a particle. If there are few pixel points that do not represent the pore morphology or there are 'noise' points due to the electronic interference, then these points can be removed from the image by the de-cluttering operation to improve the accuracy and precision of the image analysis.

2.6. Thermogravimetric Analysis (TGA)

The specimens were subjected to thermogravimetric analysis using the Q5000 automatic sample processor (Figure 2) to assess the water composition and mass as a function of temperature. The mass of each powder specimen was 20 milligrams and they were ground to 140 mesh (<106 µm) while the maximum temperature applied was 400 °C. The specimens were heated with a rate of 10 °C per minute under nitrogen gas atmosphere [37].



Figure 2. Automatic sample processor for thermogravimetric analysis.

3. Results and Discussion

The existing literature [38,39] suggests that high water content can affect the quality of digital analysis, especially for rocks with relatively small pores that can retain water due to suction. For this reason, thermogravimetric (TGA) and differential (DTG) analyses were conducted to estimate the water content and type of water in the tested rock specimens.

3.1. Thermogravimetric and Differential Analysis

Figure 3 presents the outcomes of the TGA tests. The water in the rock specimen consists of tightly bound water (TBW), loosely bound water (LBW), and free water [40], with the temperature limits for water decomposition of 120 to 230 °C, 75 to 120 °C, and 25 to 75 °C, respectively [41]. The drop point in the DTG curve represents the decomposition point for water [42]. It can be inferred from Figure 1 that the water content of the sandstone and siltstone was less than 1%, while the water content of the coal was about 9% (Figure 3c). As can be seen in Figure 1, the temperature limits of free water, loosely bound water, and tightly bound water of the sandstone specimen were 38 °C, 110 °C, and 137 °C, respectively. The free water, loosely bound water, and tightly bound water temperature limits of the siltstone specimen (Figure 3b) were 48 °C, 101 °C, and 131 °C, respectively. For the coal specimen (Figure 3c), the corresponding temperature limits were 48 °C, 100 °C, and 131 °C, respectively. The results of this analysis show that the initial water content of the tested rock was low, and thus, these specimens could be used to obtain high-quality digital images.

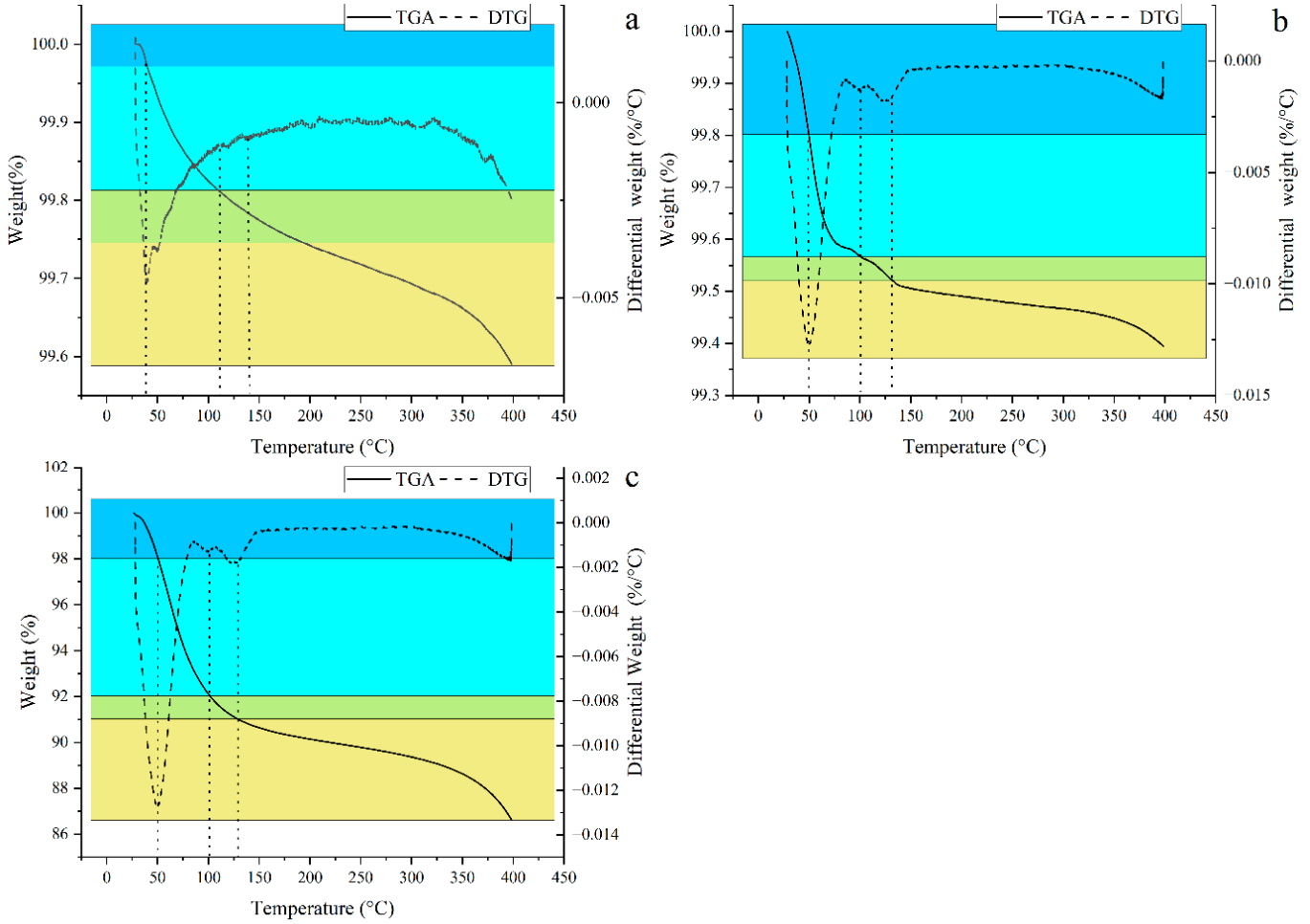

Figure 3. TGA tests results of specimens: (**a**) sandstone, (**b**) siltstone and (**c**) coal.

3.2. Mercury Intrusion Porosimetry (MIP)

The results of the MIP tests (Figure 4a) provide the reference data of the porosity and pore size diameter (PSD) for each tested rock. As the specimens were of irregular shapes, the surface features such as cracks created by the tensile fracture might have an impact on the mercury intrusion data at the low pressures applied, known as 'consistency' errors [37]. To account for this inconsistency, the comparisons between the initial mass and the mass sent back in the MIP experiments were made to identify the surface voids. The original data were then re-plotted in Figure 4b to represent the corrected pore size distributions of each rock. It is evident from Figure 4b that the MIP curves of siltstone and sandstone are similar, with the pore distribution being in the range of 1000 nm and 50,000 nm. In contrast, the pore size diameter of the coal specimen varied from 3 nm to 10,000 nm.

In the MIP test, the values of the surface tension of mercury (γ) and the contact angle of mercury (θ) were constant factors. For this reason, Equation (1) can be converted into a linear equation that relates the pressure (P) with the pore size, as given in Equation (6):

$$P = -4\gamma cos\theta/d \quad (6)$$

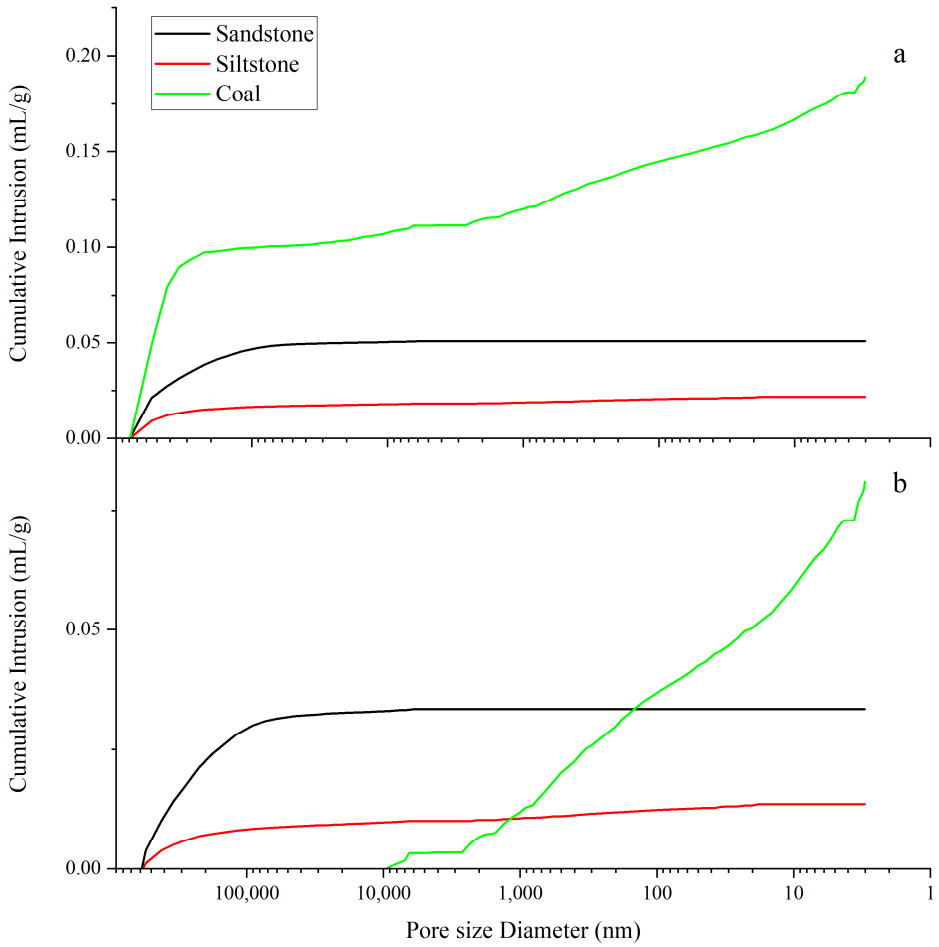

Figure 4. Results from MIP tests for sandstone, siltstone, and coal: (**a**) original data; and (**b**) data corrected to the consistency errors.

Figure 5 depicts the pore volume in 1 g of material for each pressure level and pore size. The PSD curves provide the data on the peaks and distribution of voids. It appears that the sandstone and siltstone exhibit differences in the pore size in the region of large pores (>100,000 nm), but only minor changes in the range of relatively smaller pores. For the coal specimen, a more uniform distribution of voids was observed, as shown in Figure 5. To better understand the pore distribution in the specimens, the original data were replotted in Figure 6, with the focus on the larger pore sizes, and in Figure 7, where the distribution of the smaller-sized pores was analysed. Figure 4 shows that the sandstone and siltstone have similar distribution patterns, while the data obtained for the coal specimen have the largest correction due to the effect of surface fractures and voids. The highest point in the curve is known as the most probable pore size [43], which correlates to the pore sizes that have the greatest mercury intrusion. The original data for the sandstone siltstone and coal had the same value of 700 microns as the most probable pore size. However, the modified data showed that the actual most probable pore size of the sample was smaller than the original data; that is, about 500 microns for the sandstone and siltstone, and 3 nm for the coal specimen. This difference can be attributed to two major factors: (1) the consistency errors, and (2) the presence of a certain amount of voids smaller than 3 nm in the coal specimen. Figure 7a shows that no change in the pore size diameter for the sandstone was observed at 6000 nm, while for the siltstone, this occurred at approximately 15 nm (Figure 7b).

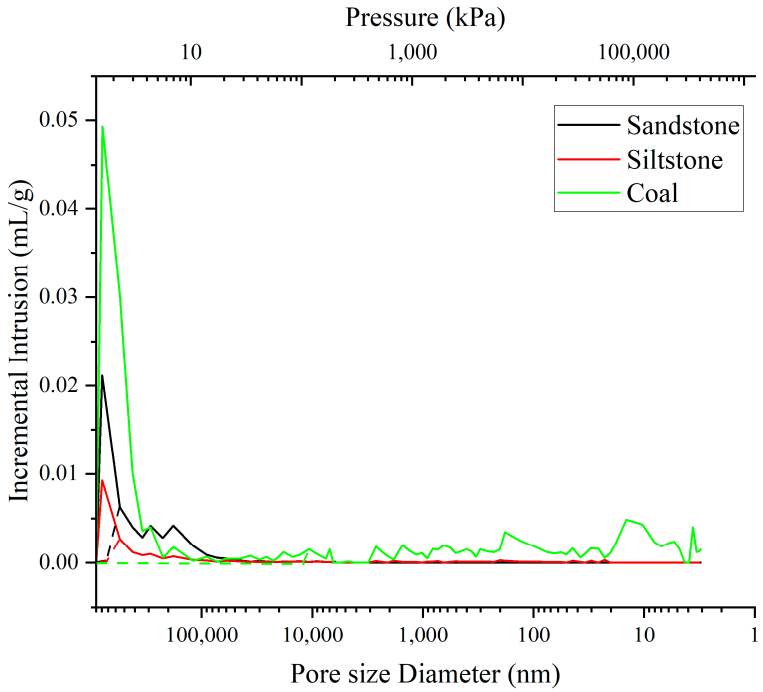

Figure 5. Incremental intrusion results from MIP for sandstone, siltstone, and coal (dashed lines denote the modified/corrected data).

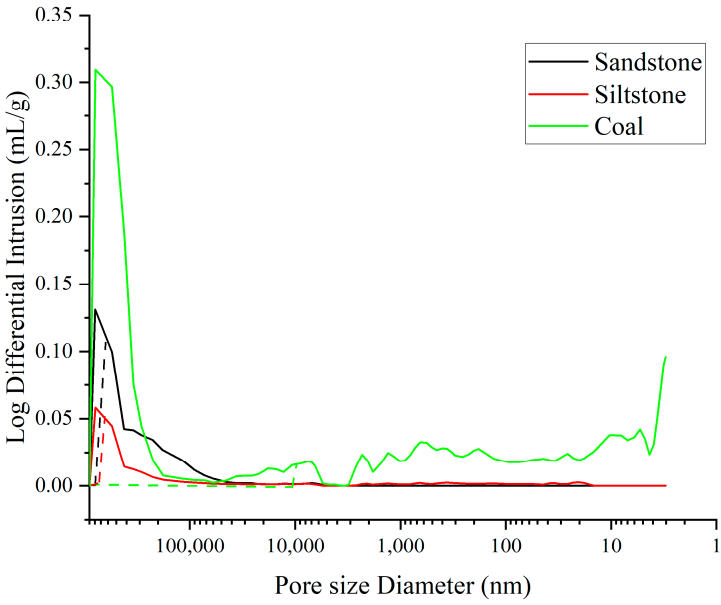

Figure 6. Experimental data plotted as the log differential intrusion against the pore size diameters of sandstone, siltstone, and coal (dashed lines denote the modified/corrected data).

Three types of sedimentary samples were examined in this study using high-pressure mercury intrusion porosimetry (MIP). The two different advanced mathematical forms of MIP data presentation, differential pore volume versus diameter (*DV/Dd*), and the log differential pore volume versus diameter (*DV/Dlogd*) were used to analyse pore size distribution. The findings of the comparison revealed a difference in the range of pore size diameter. For example, smaller pore ranges would be encouraged by the *DV/Dd* curve, but greater pore ranges would be encouraged by the *DV/Dlogd* curve. Additionally, the *DV/Dlogd* approach is appropriate for all specimens, and the *DV/Dd* approach is only appropriate for the coal specimen.

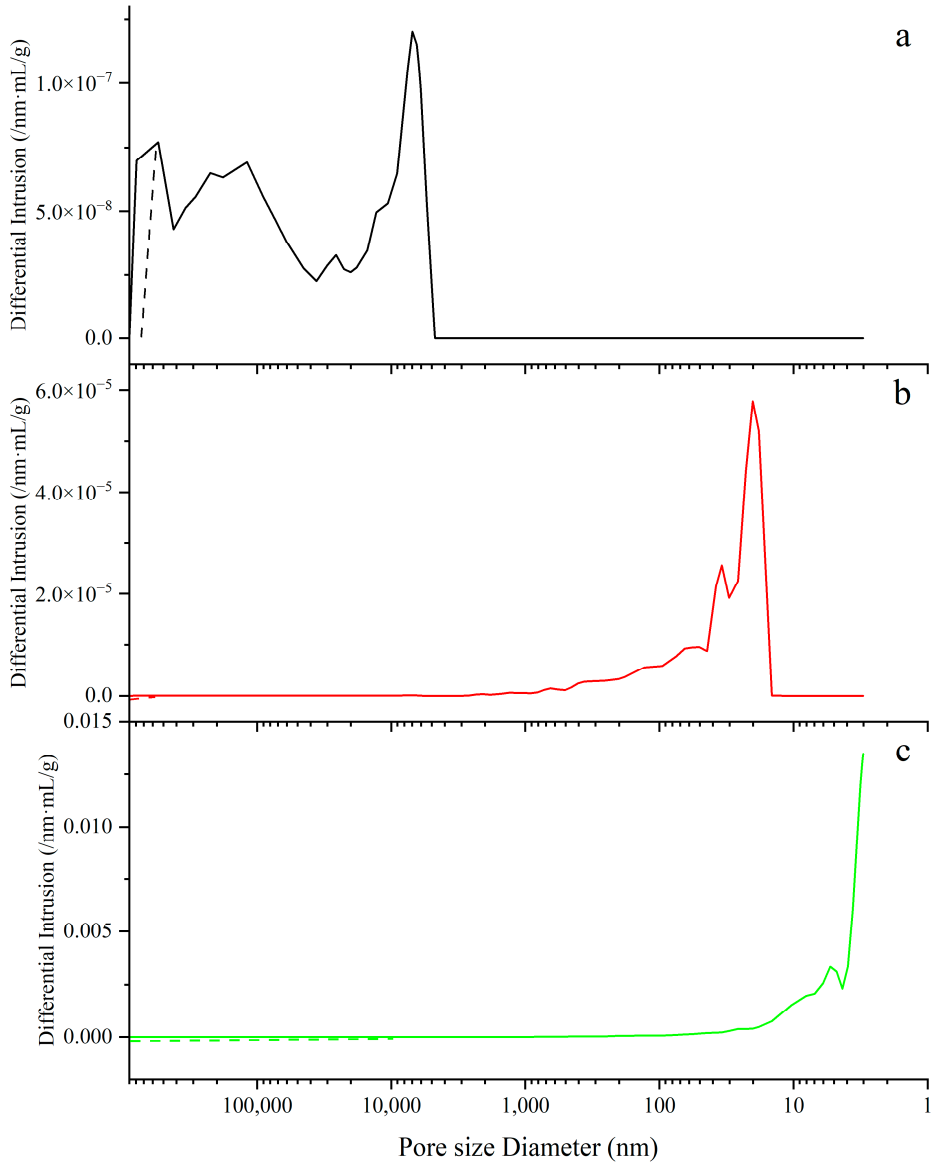

Figure 7. Experimental data plotted as the differential intrusion against the pore size diameters of sandstone (**a**), siltstone (**b**), and coal (**c**) (dashed line represents the corrected data).

3.3. Scanning Electron Microscope (SEM) and Pore and Crack Analysis System (PCAS)

Scanning electron microscope images of each rock specimen are given in Figure 6. Upon examination of these images, the voids and fissures can be clearly identified as distinct black areas. The following observations can be made for each rock type:

- The SEM image surface of the sandstone contains a variety of mineral crystal particles such as kaolinite, calcite, and quartz, with a large number of intergranular pores and microcracks, mainly distributed around the mineral crystals. At a 500× magnification (Figure 8a), the voids and quartz mineral grains can be clearly observed to be uniformly distributed over the entire sample surface. At a magnification of 10,000 (Figure 8d), the quartz grains appear to be of different sizes, with more visible kaolinite particles (flakes), and an increasing porosity space. Under a greater magnification of 30,000× (Figure 8g), the kaolinite particles between the sandstone grains can be clearly identified. Moreover, it is evident that the kaolinite flakes are being sandwiched between the quartz minerals, and a small amount of calcite adhering to the kaolinite and quartz can be recognized.

- The siltstone is mostly made of larger-sized quartz grains and kaolinite particles that create intergranular pores with a large pore area. At a 500× magnification (Figure 8b), a large number of kaolinite flakes can be clearly observed on the surface of the quartz, with a relatively large amount of voids formed between these flakes. The pore space appears to be evenly distributed. As can be seen in the image with the 10,000× magnification (Figure 8e), the kaolinite particles/aggregates are located on the quartz grains. At the 30,000× magnification (Figure 8h), the kaolinite flakes are attached to the smooth quartz surfaces. The voids in the siltstone consist mainly of gaps between the quartz particles, which can be observed at every level of magnification.
- Many pores and cracks can be found on the surface of the coal specimen. At the magnification of 500x (Figure 8c), the micro cracks seem to be evenly distributed. At the magnification of 10,000× (Figure 8f), a large number of voids and cracks are also evident. At the magnification of 30,000× (Figure 8i), large micro voids can be clearly identified, which are not noticeable at the lower magnifications of 500× and 10,000×.

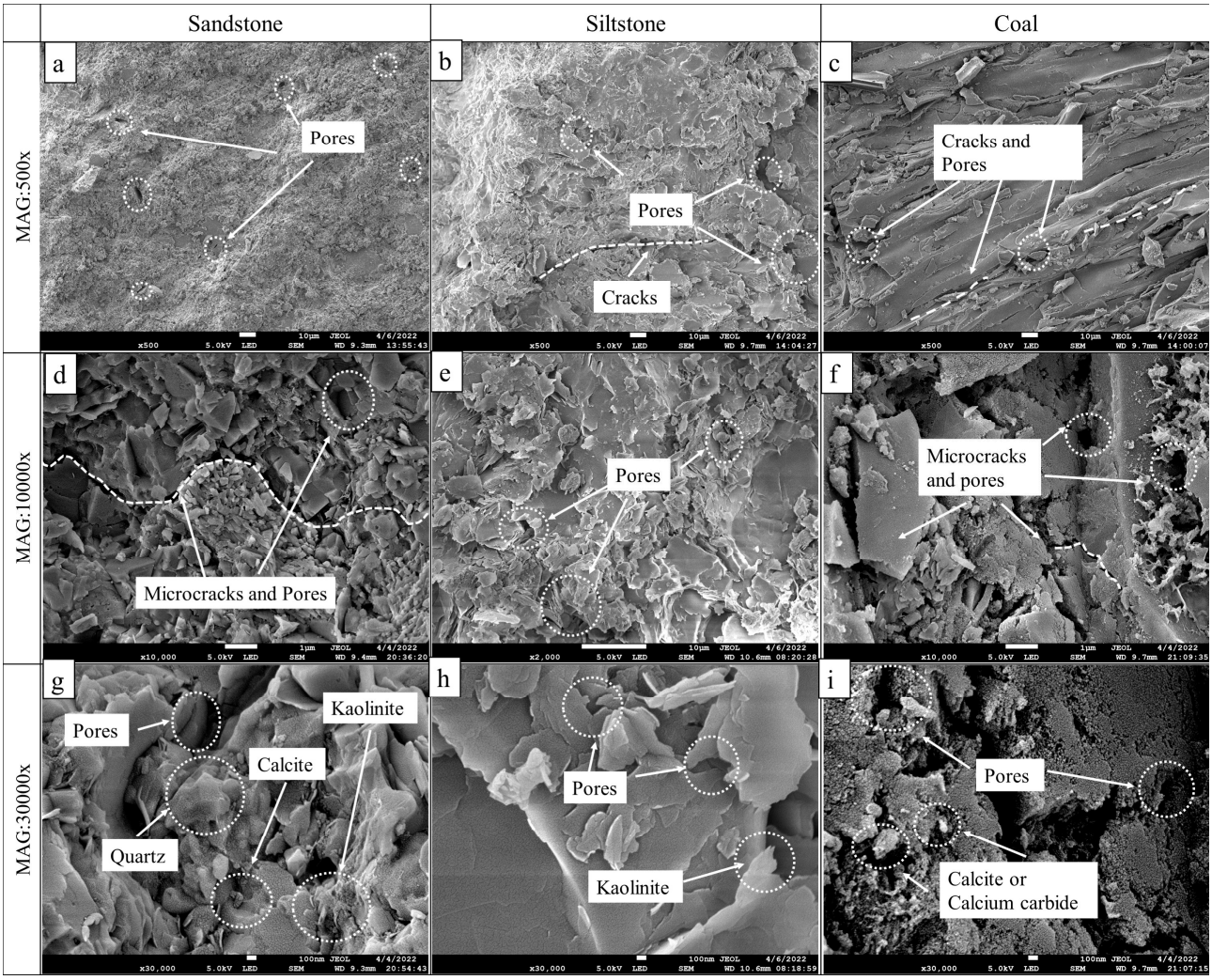

Figure 8. Scanning electron microscope images of sandstone (**a**,**d**,**g**), siltstone (**b**,**e**,**h**), and coal (**c**,**f**,**i**).

In summary, at the same magnification, the siltstone specimen displays significantly fewer fissures and voids than that of the sandstone. The coal specimen has a distinct pattern of voids and fissures compared to the sandstone and silt, with more evenly distributed voids.

By increasing the magnification around the crack area, it is possible to study the microscopic fissures and mineral characteristics of the rock. By comparing Figure 8d,g and

Figure 8e,h, it can be determined that the minimum pore size of siltstone is significantly smaller than that of sandstone. The pore size of sandstone is estimated to be around 100 nm, which agrees with the MIP data. Figure 8f,i depicts the void distribution in the coal specimen. It is evident from this figure that the voids are uniformly distributed, a finding that is also consistent with the MIP test results. It is noted that, compared to a relatively small magnification (500×), at larger magnifications such as 10,000× and 30,000×, the image analysis seems to overestimate the specimen porosity, as some 'extra' pore space (which may not exist) can be created by shadows or due to the irregular shape of pores. Experience shows that different magnifications can lead to different values of porosity [26], and thus caution needs to be taken while estimating the porosity from digital images.

The PCAS analysis of the SEM images are given in Figure 9. PCAS first determines the void space and boundaries by examining the grey colour scale (0–255) of the original SEM images (Figure 9a–c). The next stage involves the segmentation quantification and noise removal, producing a set of images (Figure 9d–f) in which the void space can be clearly identified. Comparisons of the images of the three rock specimens suggest that the void distribution in the sandstone and siltstone appears to be more uniform compared to that of the coal. Further image processing (Figure 9g–i) reveals that there is less 'noise' in the sandstone than in the siltstone and coal, and the void space in the coal is more affected by the tensile rupture at the specimen surface. This can be accounted for by the different values of porosity (Table 3) obtained from the experimental procedure (MIP) and estimated by the digital analysis using the PCAS technique. This finding seems to agree with the existing literature [13,44], which suggests that this discrepancy can be attributed to two main factors: (1) cracks and/or pores caused by the tensile damage at the surface of the specimen, and (2) different magnifications of the processed digital images.

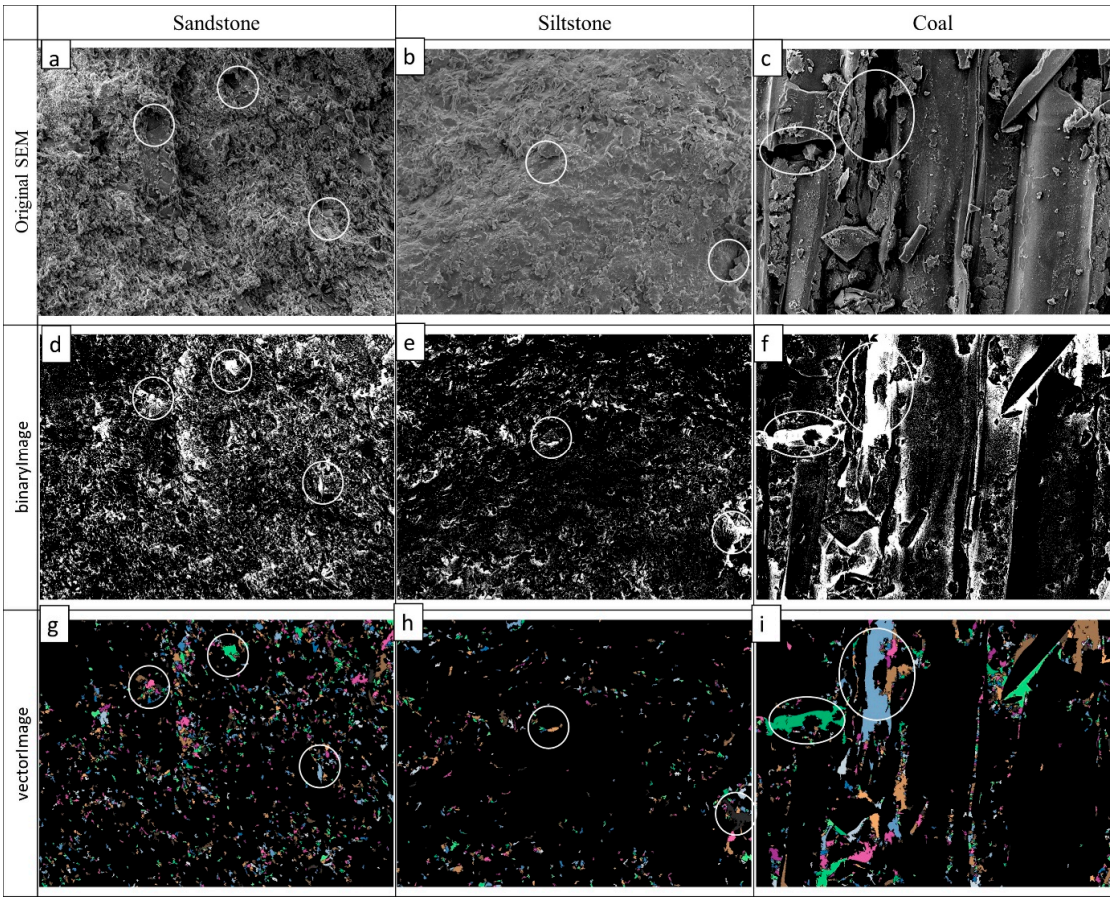

Figure 9. Pore and crack analysis system process and tensile damage of sandstone (**a**,**d**,**g**), siltstone (**b**,**e**,**h**), and coal (**c**,**f**,**i**).

Table 3. Summary of the porosity values obtained from the pore and crack analysis system and mercury intrusion porosimetry.

Rock	Pore and Crack Analysis System					Mercury Intrusion Porosimetry	
	No.	Mean (%)	Sd ± (%)	Min (%)	Max (%)	Porosity MIP Origin	Porosity MIP Modify
Sandstone	12	10.1	1.1	8.1	11.8	12.9	8.9
Siltstone	9	3.9	0.58	3.1	4.8	5.4	3.4
Coal	9	7.6	2.15	5.7	10.9	19.9	9.5

The results obtained from the experimental MIP procedure and digital analysis of SEM images by the PCAS technique are summarised in Table 3. Figure 10 demonstrates the correlation between the experimental (MIP) and PCAS data obtained for all three rock specimens. The upper and lower boundaries and the median value of multipliers obtained through the analysis of the existing literature (Table 1) are given in this figure as well. The data from this study seem to fit well within the range reported in the literature. The previous data on different types of sandstone and siltstone [24,27,31] give a relatively narrow range of multipliers (from 0.94 to 1.21) that can be used to estimate the rock porosity based on the digital image analysis. The results of this study suggest a value of 0.88, which seems to fit reasonably well with the previous research. These consistent results obtained for sandstone/siltstone by different researchers can be due to the mineral composition of these rocks (that is, quartz is the dominant mineral), which is associated with relatively uniform pore space in the micron range.

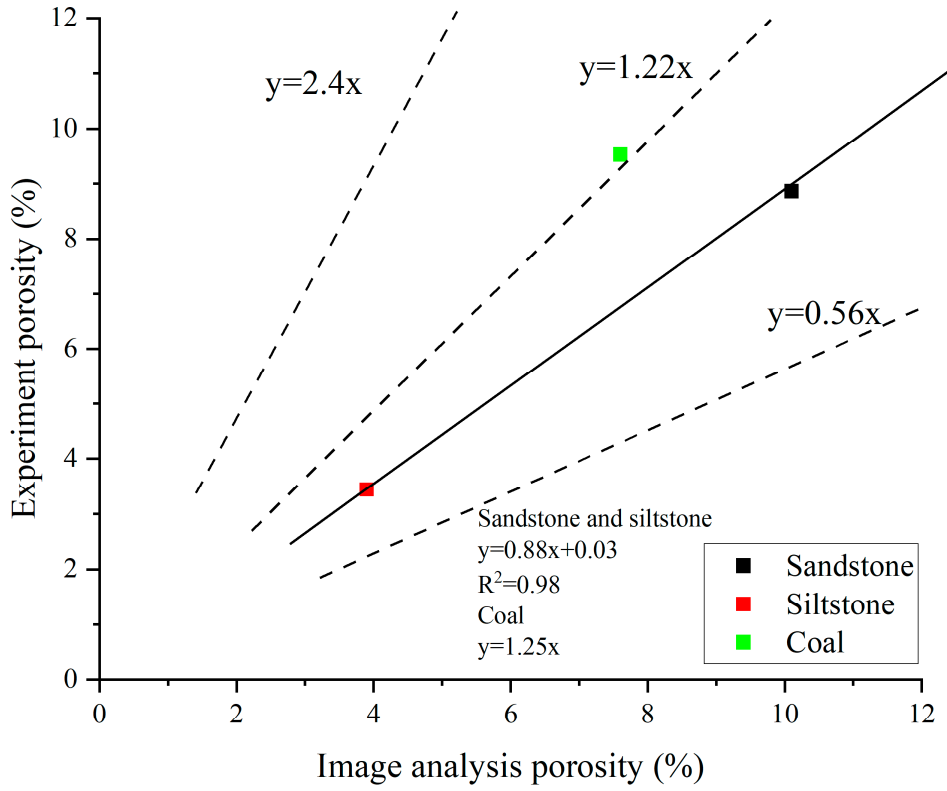

Figure 10. Correlations between the porosity values obtained from the image analysis and laboratory experiments for the sandstone, siltstone, and coal.

However, there are still some limitations that need to be considered [15,24,27]. The first is related to the precision of MIP tests, as it may be challenging to accurately estimate

the mercury intrusion in the pore space [37,45]. Second, the pore space and microcracks observed in SEM images may be different from those in reality because the SEM images only identify 2D types of pore space, compared to the 3D pore space obtained from MIP experiments [15,26]. Third, the greyscale level threshold values used for the SEM image analysis and the image resolution can have an impact on the final results as well [27].

4. Conclusions

The porosity of three different rocks (sandstone, siltstone, and coal) were studied using a series of laboratory tests (MIP) and digital analysis using high-quality SEM images and the PSAC technique. Based on the obtained results, the following major conclusions can be drawn:

- The majority of sandstone and siltstone pores were larger than 1000 nm in diameter. The sandstone had a minimum pore size of 3000 nm, while the siltstone had a minimum pore size of around 15 nm. The coal pore size was found to be linear between 10,000 nm and 3 nm, according to the MIP test in which the maximum pressure of 400 MPa was applied. Furthermore, DV/Dd is more appropriate to be used for characterizing PSD data for sedimentary rock.
- The data from the SEM image agree with the results from the MIP tests. The minimal pore size of sandstone was around 1000 nm, whereas the minimum pore size of the siltstone was approximately 10 nm.
- The linear relationship between the two-dimensional porosity (from PACS) and the three-dimensional porosity (from MIP) seems to exist with a multiplier of 0.88 for the sandstone and siltstone. For these two rocks, quartz was the dominant mineral, which created uniform void space.

The combination of PACS analysis and MIP tests can provide useful insights into the pore size distribution of rock. However, inconsistences (especially for more porous rocks like coal) can exist when SEM images at higher magnifications are analysed. In this case, the porosity obtained from the image analysis appears greater than the porosity measured in the laboratory. Overall, the results can be processed directly in the field of rock science, or as a preparation or comparative phase for in-depth research, saving time and effort and enhancing the precision of tests. Here, it is useful to select photographs that require appropriate magnification, since these images will have a significant impact on the data inaccuracy.

Author Contributions: Conceptualization, Q.T. and I.G.; methodology, Q.T.; software, Q.T.; validation, Q.T. and I.G.; formal analysis, Q.T.; investigation, Q.T.; resources, I.G.; data curation, Q.T.; writing—original draft preparation, Q.T.; writing—review and editing, I.G.; visualization, Q.T.; supervision, I.G.; project administration, I.G.; funding acquisition, I.G. All authors have read and agreed to the published version of the manuscript.

Funding: This research received no external funding.

Institutional Review Board Statement: Not applicable.

Informed Consent Statement: Not applicable.

Data Availability Statement: The data that support the findings of this study are available from the corresponding author upon reasonable request.

Conflicts of Interest: The authors declare no conflict of interest.

References

1. Schöpfer, M.P.J.; Abe, S.; Childs, C.; Walsh, J.J. The impact of porosity and crack density on the elasticity, strength and friction of cohesive granular materials: Insights from DEM modelling. *Int. J. Rock Mechan. Min. Sci.* **2009**, *46*, 250–261. [CrossRef]
2. Labani, M.M.; Rezaee, R.; Saeedi, A.; Al Hinai, A. Evaluation of pore size spectrum of gas shale reservoirs using low pressure nitrogen adsorption, gas expansion and mercury porosimetry: A case study from the Perth and Canning Basins, Western Australia. *J. Petrol. Sci. Eng.* **2013**, *112*, 7–16. [CrossRef]

3. Baud, P.; Wong, T.F.; Zhu, W. Effects of porosity and crack density on the compressive strength of rocks. *Int. J. Rock Mechan. Min. Sci.* **2014**, *67*, 202–211. [CrossRef]
4. Anovitz, L.M.; Cole, D.R. Characterization and Analysis of Porosity and Pore Structures. *Pore-Scale Geochem. Proc.* **2015**, *80*, 61. [CrossRef]
5. Gao, F.; Hu, Y.H.; Liu, G.N.; Yang, Y.G. Experiment Study on Topological Characteristics of Sandstone Coating by Micro CT. *Coatings* **2020**, *10*, 1143. [CrossRef]
6. Hawkes, I.; Mellor, M. Uniaxial Testing in Rock Mechanics Laboratories. *Eng. Geol.* **1970**, *4*, 177. [CrossRef]
7. Vernik, L.; Bruno, M.; Bovberg, C. Empirical Relations between Compressive Strength and Porosity of Siliciclastic Rocks. *Int. J. Rock Mechan. Min. Sci. Geomechan. Abstracts* **1993**, *30*, 677–680. [CrossRef]
8. Chang, C.D.; Zoback, M.D.; Khaksar, A. Empirical relations between rock strength and physical properties in sedimentary rocks. *J. Petrol. Sci. Eng.* **2006**, *51*, 223–237. [CrossRef]
9. Fang, X.L.; Cai, Y.D.; Liu, D.M.; Zhou, Y.F. A Mercury Intrusion Porosimetry Method for Methane Diffusivity and Permeability Evaluation in Coals: A Comparative Analysis. *Appl. Sci.* **2018**, *8*, 860. [CrossRef]
10. Abell, A.B.; Willis, K.L.; Lange, D.A. Mercury Intrusion Porosimetry and Image Analysis of Cement-Based Materials. *J. Colloid Interf. Sci.* **1999**, *211*, 39–44. [CrossRef]
11. Igarashi, S.; Watanabe, A.; Kawamura, M. Evaluation of capillary pore size characteristics in high-strength concrete at early ages. *Cement Concrete Res.* **2005**, *35*, 513–519. [CrossRef]
12. İnan Sezer, G.; Ramyar, K.; Karasu, B.; Burak Göktepe, A.; Sezer, A. Image analysis of sulfate attack on hardened cement paste. *Mater. Design* **2008**, *29*, 224–231. [CrossRef]
13. Chalmers, G.R.; Bustin, R.M.; Power, I.M. Characterization of gas shale pore systems by porosimetry, pycnometry, surface area, and field emission scanning electron microscopy/transmission electron microscopy image analyses: Examples from the Barnett, Woodford, Haynesville, Marcellus, and Doig units. *Aapg Bullet.* **2012**, *96*, 1099–1119. [CrossRef]
14. Lai, J.; Wang, G.W.; Wang, Z.Y.; Chen, J.; Pang, X.J.; Wang, S.C.; Zhou, Z.L.; He, Z.B.; Qin, Z.Q.; Fan, X.Q. A review on pore structure characterization in tight sandstones. *Earth-Sci. Rev.* **2018**, *177*, 436–457. [CrossRef]
15. Loucks, R.G.; Reed, R.M.; Ruppel, S.C.; Jarvie, D.M. Morphology, Genesis, and Distribution of Nanometer-Scale Pores in Siliceous Mudstones of the Mississippian Barnett Shale. *J. Sedim. Res.* **2009**, *79*, 848–861. [CrossRef]
16. Jiao, K.; Yao, S.P.; Liu, C.; Gao, Y.Q.; Wu, H.; Li, M.C.; Tang, Z.Y. The characterization and quantitative analysis of nanopores in unconventional gas reservoirs utilizing FESEM-FIB and image processing: An example from the lower Silurian Longmaxi Shale, upper Yangtze region, China. *Int. J. Coal Geol.* **2014**, *128*, 1–11. [CrossRef]
17. Li, L.; Huang, B.; Tan, Y.; Deng, X.; Li, Y.; Zheng, H. Geometric Heterogeneity of Continental Shale in the Yanchang Formation, Southern Ordos Basin, China. *Sci. Rep.* **2017**, *7*, 6006. [CrossRef]
18. Tang, C.S.; Shi, B.; Cui, Y.J.; Liu, C.; Gu, K. Desiccation cracking behavior of polypropylene fiber-reinforced clayey soil. *Can. Geotech. J.* **2012**, *49*, 1088–1101. [CrossRef]
19. Sadasivam, B.Y.; Reddy, K.R. Adsorption and transport of methane in landfill cover soil amended with waste-wood biochars. *J. Environ. Manag.* **2015**, *158*, 11–23. [CrossRef]
20. Sadasivam, B.Y.; Reddy, K.R. Engineering properties of waste wood-derived biochars and biochar-amended soils. *Int. J. Geotech. Eng.* **2015**, *9*, 521–535. [CrossRef]
21. Yu, Y.; Chen, N.; Hu, W.W.; Feng, C.P. Application of Taguchi experimental design methodology in optimization for adsorption of phosphorus onto Al/Ca-impregnated granular clay material. *Desal. Water Treat.* **2015**, *56*, 2994–3004. [CrossRef]
22. Liu, C.; Wang, B.J.; Shi, B.; Tang, C.S. Analytic method of morphological parameters of cracks for rock and soil based on image processing and recognition. *Chin. J. Geotech. Eng.* **2008**, *30*, 1383–1388.
23. Liu, C.; Tang, C.S.; Shi, B.; Suo, W.B. Automatic quantification of crack patterns by image processing. *Comput. Geosci.* **2013**, *57*, 77–80. [CrossRef]
24. Desbois, G.; Urai, J.L.; Kukla, P.A.; Konstanty, J.; Baerle, C. High-resolution 3D fabric and porosity model in a tight gas sandstone reservoir: A new approach to investigate microstructures from mm- to nm-scale combining argon beam cross-sectioning and SEM imaging. *J. Petrol. Sci. Eng.* **2011**, *78*, 243–257. [CrossRef]
25. Bera, B.; Gunda, N.S.; Mitra, S.K.; Vick, D. Characterization of nanometer-scale porosity in reservoir carbonate rock by focused ion beam-scanning electron microscopy. *Microsc. Microanal* **2012**, *18*, 171–178. [CrossRef] [PubMed]
26. Klaver, J.; Desbois, G.; Urai, J.L.; Littke, R. BIB-SEM study of the pore space morphology in early mature Posidonia Shale from the Hils area, Germany. *Int. J. Coal Geol.* **2012**, *103*, 12–25. [CrossRef]
27. Guan, K.M.; Nazarova, M.; Guo, B.; Tchelepi, H.; Kovscek, A.R.; Creux, P. Effects of Image Resolution on Sandstone Porosity and Permeability as Obtained from X-ray Microscopy. *Trans. Porous Media* **2019**, *127*, 233–245. [CrossRef]
28. Lyu, K.; She, W.; Miao, C.W.; Chang, H.L.; Gu, Y. Quantitative characterization of pore morphology in hardened cement paste via SEM-BSE image analysis. *Construct. Build. Mater.* **2019**, *202*, 589–602. [CrossRef]
29. Sun, H.F.; Belhaj, H.; Tao, G.; Vega, S.; Liu, L.F. Rock properties evaluation for carbonate reservoir characterization with multi-scale digital rock images. *J. Petrol. Sci. Eng.* **2019**, *175*, 654–664. [CrossRef]
30. Goral, J.; Andrew, M.; Olson, T.; Deo, M. Correlative core- to pore-scale imaging of shales. *Mar. Petrol. Geol.* **2020**, *111*, 886–904. [CrossRef]

31. Niu, Y.F.; Wang, Y.D.; Mostaghimi, P.; Swietojanski, P.; Armstrong, R.T. An Innovative Application of Generative Adversarial Networks for Physically Accurate Rock Images With an Unprecedented Field of View. *Geophys. Res. Lett.* **2020**, *47*. [CrossRef]
32. Kim, D.H.; Gratchev, I.; Balasubramaniam, A. Determination of joint roughness coefficient (JRC) for slope stability analysis: A case study from the Gold Coast area, Australia. *Landslides* **2013**, *10*, 657–664. [CrossRef]
33. Bass, J.D. Elasticity of minerals, glasses, and melts. *Miner. Phys. Crystallogr. Handbook Phys. Constants* **1995**, *2*, 45–63.
34. Vidana Pathiranagei, S.; Gratchev, I.; Sokolowski, K.A. Investigation of the microstructural characteristics of heated sandstone by micro-computed tomography technique. *Environ. Earth Sci.* **2022**, *81*. [CrossRef]
35. AQSIQ; SAC. *GB/T 21560.1-2008*; Pore Size Distribution and Porosity of Solid Materials by Mercury Porosimetry and Gas Adsorption—Part 1: Mercury Porosimetry. 2008.
36. Liu, K.; Ostadhassan, M. The impact of pore size distribution data presentation format on pore structure interpretation of shales. *Adv. Geo-Energy Res.* **2019**, *3*, 187–197. [CrossRef]
37. Sigal, R.F. A methodology for blank and conformance corrections for high pressure mercury porosimetry. *Meas. Sci. Technol.* **2009**, *20*, 045108. [CrossRef]
38. Liu, Y.F.; Shi, Y.H.; Yang, H.E.; Wu, T.J.; Liu, X.; Liu, S.; Zhou, D.S. Visualisation and investigation of water retention in tight oil reservoir via real sandstone micro-models. *Int. J. Oil Gas Coal Technol.* **2021**, *27*, 111–126. [CrossRef]
39. Inoue, N.; Takashima, Y.; Suga, M.; Suzuki, T.; Nemoto, Y.; Takai, O. Observation of wet specimens sensitive to evaporation using scanning electron microscopy. *Microscopy* **2018**, *67*, 356–366. [CrossRef]
40. Wang, M.; Wen, J.M.; Zhuang, H.; Xia, W.Y.; Jiang, N.J.; Du, Y.J. Screening Additives for Amending Compacted Clay Covers to Enhance Diffusion Barrier Properties and Moisture Retention Performance. *Appl. Sci.* **2022**, *12*, 7341. [CrossRef]
41. Wang, Y.J.; Lu, S.; Ren, T.S.; Li, B.G. Bound Water Content of Air-Dry Soils Measured by Thermal Analysis. *Soil Sci. Soc. Am. J.* **2011**, *75*, 481–487. [CrossRef]
42. Labus, K.; Labus, M. Thermogravimetry as a tool for measuring of fracturing fluid absorption in shales. *J. Therm. Anal. Calorim.* **2018**, *133*, 919–927. [CrossRef]
43. Zhang, Z.L.; Cui, Z.D. Effects of freezing-thawing and cyclic loading on pore size distribution of silty clay by mercury intrusion porosimetry. *Cold Regions Sci. Technol.* **2018**, *145*, 185–196. [CrossRef]
44. Nelson, P.H. Pore-throat sizes in sandstones, tight sandstones, and shales. *Aapg Bullet.* **2009**, *93*, 329–340. [CrossRef]
45. Hildenbrand, A.; Urai, J.L. Investigation of the morphology of pore space in mudstones—First results. *Mar. Petrol. Geol.* **2003**, *20*, 1185–1200. [CrossRef]

Disclaimer/Publisher's Note: The statements, opinions and data contained in all publications are solely those of the individual author(s) and contributor(s) and not of MDPI and/or the editor(s). MDPI and/or the editor(s) disclaim responsibility for any injury to people or property resulting from any ideas, methods, instructions or products referred to in the content.